JOURNAL OF AIRCRAFT
Vol. 35, No. 6, November–December 1998

Characterization of the Flowfield near a Wrap-Around Fin at Mach 2.8

C. P. Tilmann*
U.S. Air Force Research Laboratory, Wright–Patterson Air Force Base, Ohio 45433-7913
T. A. Buter†
U.S. Air Force Test Pilot School, Edwards Air Force Base, California 93524-6485
and
R. D. W. Bowersox‡
University of Alabama, Tuscaloosa, Alabama 35487-0280

The Navier–Stokes equations have been solved in the vicinity of a single wrap-around fin mounted on a semicylindrical missile body shape with the objective of quantifying the flow structure in the region near the fin/body juncture (Mach number 2.8, unit Reynolds number $18 \times 10^6\ \mathrm{m}^{-1}$). The Baldwin–Lomax algebraic eddy viscosity model was employed. Correlation with experimental data suggests that the calculations have captured the principal features of this complicated flowfield. The calculations, corroborated by experimental results, indicate that a vortex exists in the fin/body juncture region on the convex side of the fin. This vortex, not predicted in previous inviscid simulations, can greatly influence the pressure loading on the fin near the root. Changes in this vortex structure may contribute to the rolling moment reversal observed at high supersonic speeds in recent flight-test experiments.

Nomenclature

c	=	chord length of missile fin, 2.03 cm
l	=	reference length
M	=	Mach number
P_{t2}	=	pitot pressure
$P_{t\infty}$	=	plenum total pressure
r	=	model fin radius of curvature, 1.59 cm
u, v, w	=	mean Cartesian velocity components
x, y, z	=	Cartesian coordinates
Y	=	distance from body surface in y direction
y^+	=	inner turbulent coordinate $yu_\tau\rho/\mu$, $u_\tau^2 = \tau_w/\rho_w$
δ_0	=	reference boundary-layer thickness, 6.1 mm
θ	=	horizontal flow angularity, $\tan^{-1}(v/u)$
ρ	=	density
ϕ	=	azimuthal flow angularity, $\tan^{-1}(w/u)$
∞	=	subscript, freestream condition

Introduction

THE term ''wrap-around fin'' (WAF) usually refers to a projectile stabilizing or control surface, which has the same curvature as the missile body, and is wrapped around the projectile until deployment. Because stealth capability has become a design parameter for many aircraft, WAFs have become even more attractive for their reduced cross section and stowability. WAFs can also simplify the design of airframes that integrate the weapon in partial concealment, avoiding complications associated with fin–body contact. However, rolling- and side-moment reversals have been observed during ballistic range tests over a small range of high supersonic speeds ($M \approx 4.5$–4.7) on a WAF configuration.[1,2] This phenomenon has not yet been reproduced using computational methods. The majority of previous WAF experiments have focused on characterizing stability characteristics via subscale flight tests, usually in the subsonic and transonic flight regimes. While these experiments have identified the unusual stability characteristics of WAFs, they have not provided an understanding of the flowfield. Numerical simulations have also been performed on wrap-around finned missiles. Of these simulations, the majority has been focused on characterizing the fin shock structures and the interactions between fins. This has typically been done using inviscid computational fluid dynamics (CFD) methods on configurations with fins of little or no thickness,[2,3] or neglecting turbulent effects.[4]

The primary goal of the present research was to characterize the flow structure near WAFs at a supersonic condition. This has been accomplished through a systematic numerical and experimental study of the mean and turbulent flowfield in the vicinity of a single WAF. An understanding of the flowfield near WAFs is critical to the further development of such configurations, given the dependence of stability characteristics on Mach number. Determination of the flow structure near a single nonspinning WAF is an essential first step toward this understanding.

As a first step toward understanding the flow structure near WAFs, a simple model consisting of a single WAF mounted on a partial body was investigated in the U.S. Air Force Institute of Technology (AFIT) Mach 3 tunnel.[5–8] This simplified model allowed experimental data to be obtained at much higher resolution than would have been possible on a full-body four-finned configuration scaled to fit in the available tunnel space. Also, the single-WAF static model isolated the effects of fin curvature from the effects of upstream crossflow and interaction of the multiple fin shocks. Although this experimental investigation produced a significant amount of mean flow and turbulence data not previously available,[8] the subsequent application of CFD has provided a much more complete understanding of the flowfield. The numerical results were obtained by solving the Reynolds-averaged Navier–Stokes (RANS) equations, with an algebraic turbulence model, over

Received Feb. 22, 1998; revision received July 7, 1998; accepted for publication July 8, 1998.

*Research Engineer, Aeronautical Sciences Division, Air Vehicles Directorate, AFRL/VAAA, 2645 5th Street, Suite 7. Senior Member AIAA.

†Research Director, 220 South Wolfe Avenue. Senior Member AIAA.

‡Assistant Professor, Department of Aerospace Engineering and Mechanics, Box 870280. Senior Member AIAA.

the single-WAF model geometry.[7,9] Solutions were obtained with a widely used commercial simulation package (the General Aerodynamic Simulation Program, GASP[10]), and the numerical results compared with the experimental results. These simulations were conducted at the experimental flow conditions of Mach number 2.80, with a settling chamber total pressure and total temperature of 2.14 ± 0.02 atm and 294 ± 2 K, respectively. Taken in concert, the experimental and numerical information is examined with a view toward characterizing the net effect of the complex flowfield in the vicinity of the WAF on aerodynamic loading.

Numerical Method

The entire computational mesh consisted of 12 computational zones (the edges of which are shown in Fig. 1), connected by 21 zonal boundaries and composed of 8.2×10^6 cells. The flow variable values were passed through the zonal boundaries via five-point overlaps. The algebraic eddy viscosity model of Baldwin and Lomax[11] was used to approximate turbulence. To resolve the features of the flowfield in the vicinity of the fin, and to provide the resolution required by the turbulence model, the grid was clustered near the fin and body surfaces. At a location $0.41c$ upstream of the fin leading edge, the first grid point from the body (the center of the first cell) was at a y^+ value of roughly 0.45, and more than half of the points were contained in the boundary layer.

Solution Strategy

Because flow disturbances do not propagate upstream in a fully supersonic flow, and because experimental results indicated that the blended body produced no separated flow regions, the parabolized Navier–Stokes (PNS) equations were solved to a location $0.5c$ ahead of the fin. This location was deemed sufficiently far upstream of the fin interaction region based on previously conducted visualization experiments.[5,6,8]

To allow for the specification of a one-dimensional upstream boundary condition, the PNS equations were solved on a two-dimensional grid for a short distance ($0.8r$) ahead of the model body. Flow conditions at the inflow boundary were prescribed using experimental data from pitot, cone-static, and hot-film surveys. Owing to probe volume effects, experimental data could not be obtained sufficiently close to the wall to include the viscous sublayer (the first measurement point was at an estimated y^+ value on the order of 100–200). However, the two-dimensional PNS region allowed the boundary layer to develop into a fully turbulent profile upstream of the blended body region. The two dimensionality of the flow in the AFIT Mach 3 wind tunnel has been well documented.[5,12]

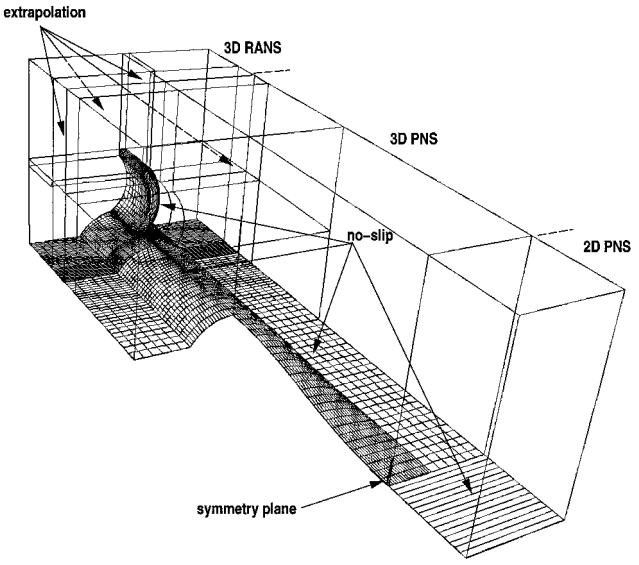

Fig. 1 Grid boundaries and zonal structure for viscous numerical simulations. Every fourth grid line shown on no-slip boundaries.

The flat-plate solution at the exit of this two-dimensional zone was mapped to the three-dimensional grid at the leading edge of the blended body. The two-factor approximately factorized PNS equations were solved at each marching plane by employing a third-order upwind-biasing scheme with relaxation in the marching direction and a second-order upwind scheme with Roe's flux difference splitting in the crossflow plane.[10] The symmetry of the model body was exploited by solving the governing equations over only half of the blended body region and enforcing symmetry at the $z = 0$ plane. GASP was modified to allow the solution at the final symmetric marching plane to be reflected across the $z = 0$ plane. The solution at this plane was then used as the upstream condition for the downstream asymmetric region (behind the plane at $0.5c$ ahead of the fin), where the RANS equations were solved to third-order spatial accuracy using Jacobi inner iterations.[10] The inviscid fluxes were split by the method of van Leer,[13] and the min–mod limiter[10] was used. This region is composed of eight computational zones, containing a total of 4.2×10^6 cells.

On the model surfaces, shown as a mesh in Fig. 1, a no-slip condition on the velocity, an isothermal wall temperature (294 K), and vanishing normal pressure gradient were enforced. The solid surface boundary conditions were enforced explicitly to second-order accuracy with a full flux method.[10] Based on the results of our previous experiments and inviscid numerical investigation,[5,6,8] it was known that the side and opposing tunnel walls had a minimal influence on the flowfield near the fin. Thus, although the size of the computational domain represents the test section, flow conditions were extrapolated from the interior at these boundaries, affording great computational savings. The flow conditions were also extrapolated at the downstream plane.

Convergence Issues

A three-grid sequencing method was used that not only substantially reduced computational time by starting the solution on a much coarser grid, but also afforded an expedient means to evaluate grid consistency.[7,9] Temporal convergence was demonstrated on each grid by recording the solution on lines corresponding to experimental surveys. When the solution stopped changing with further integration, the Euclidean norm of the residual vector was typically reduced by three to four orders of magnitude.[7,9]

In the space-marched region ($x \leq -0.5c$), though sequencing would not accelerate convergence, solutions were obtained on all three grids simply to evaluate grid consistency. Comparison of the solutions at the exit of this region indicated that the maximum difference in the predicted boundary layers on the two finest grids was on the order of 1%.[7–9] Because it was thought that the implementation of algebraic closure models in regions having more than one physical length scale may cause convergence difficulties (particularly on the coarser grids), the grid convergence studies were conducted by solving the laminar form of the RANS equations in the fin region.[7,9]

Examination of the vortical structures ahead of the fin leading edge ($x/c \leq 0$, see Fig. 2) has indicated that the structure of the flowfield obtained on the coarsest grid is unlike that predicted on the two finer grids.[7,9] While the solution on the coarsest grid contained only one vortex pair ahead of the fin, the first grid refinement yielded a four-vortex structure, and the final grid refinement moved the predicted locations of these vortices slightly toward the fin. It is important to recognize that this region is the most difficult area of the flowfield to resolve, because the flow character is changing drastically over short distances. Also, because these particular vortical structures are swept away from the fin, minimizing the effects of their inner composition on the fin loading, it is probably not

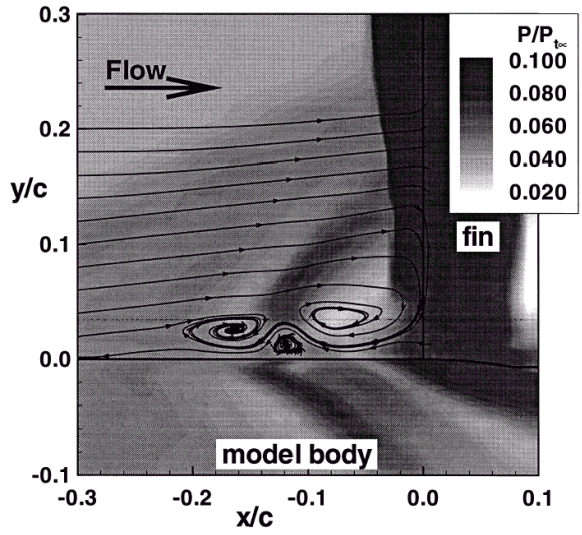

Fig. 2 Computed vortical structure ahead of the fin.

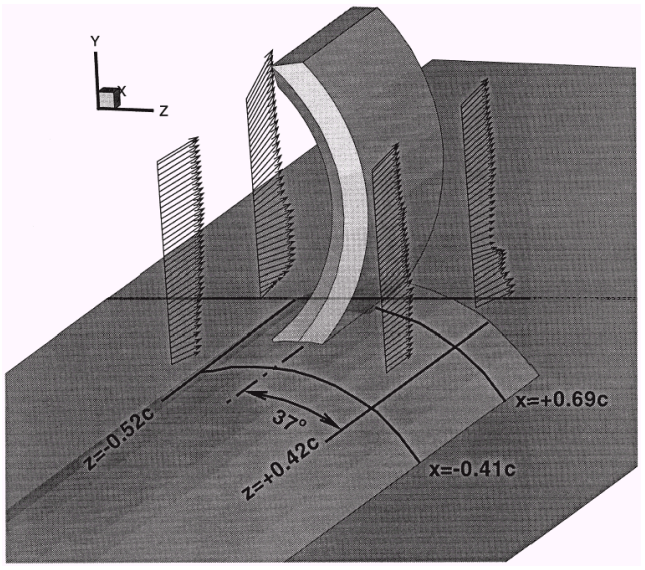

Fig. 3 Probe locations.

necessary to resolve this region of the flow precisely.[7] In the present simulations, while the predicted flowfield ahead of the fin is slightly altered by the last grid refinement, the flowfield behind the interaction region and the pressures on the fin surface are essentially unchanged. Predicted rolling moment coefficients calculated by integrating the surface pressures on the fin sides for the two finest meshes agree within 0.2%, indicating that grid convergence was achieved in the region of interest.[7,9]

Computational Requirements

As expected, the computational requirements for the RANS calculations (fin region), both in terms of the memory and CPU, increase by approximately a factor of 8 with each grid refinement. For the finest grid (4.17×10^6 cells), GASP required 113×10^6 Words of memory and 134 s/iteration on a Cray C916 computer when the Baldwin–Lomax turbulence model was employed. An entire calculation required on the order of 120 CPU hours. Details of the computational requirements for all of the calculations are provided in Refs. 7 and 9.

Results and Discussion

It is convenient to discuss the flowfield in terms of three regions; an upstream region ahead of the fin shock, and two downstream regions, one on either side of the fin. The present study indicates that each of the downstream regions can be further divided into two regions; an outer region characterized by inviscid behavior, and an inner region near the body where viscous effects are prevalent.

Previously, the flow over this single WAF geometry has been experimentally explored by extensively probing the flowfield near the model.[5–8] As part of this investigation, the body boundary layer was surveyed at four locations on the ceiling-mounted model as shown in Fig. 3. These locations were chosen to represent the upstream and downstream regions on either side of the fin because two of the stations set the reference for the flow upstream of the fin bow shock (at $x = 0.41c$) and the other two stations were positioned downstream of the shock (at $x = +0.69c$). At each of these axial locations, the flow was surveyed with the pressure probes on the concave (Cc) side, and convex (Cv) side of the fin (at $z = \pm 0.47c$). The hot-film surveys were conducted at these same axial locations and at very near transverse locations; $z = -0.52c$ on the concave (Cc) side, and $z = +0.42c$ on the convex (Cv) side. Note that the transverse locations of the hot-film surveys had been previously reported as identical to the locations of the pressure probe surveys.[8] Based upon extensive comparison with the present numerical results and a subsequent uncertainty analysis of the experiment,[7] it is now believed that these locations are slightly different (by approximately one hot-film probe width). In the following text, results from the present numerical study are compared with the experimental data at these locations, and the combined numerical and experimental data are examined for the purpose of characterizing the flowfield.

In the data presentation, the probe position (x, y, z) is nondimensionalized by the fin chord, $c = 20.3$ mm, where the coordinate origin is located at the intersection of the body surface centerline and leading edge of the fin. Negative x values are upstream of the leading edge, and negative z values are to the concave side of the fin. Boundary-layer data are presented as functions of the distance from the model body, Y. This relative position from the body is normalized by a reference boundary-layer thickness, $\delta_0 = 6.1$ mm, which was measured on the model centerline $0.41c$ ahead of the leading edge of the fin. This thickness was defined by the distance from the surface where $M = 0.95M_e$, where Mach number was determined from pitot and cone-static data to minimize the measurement uncertainty.[8]

Flow Ahead of the Fin

At the upstream measurement location, which is ahead of the bow shock, both computed and experimental pitot pressures and mass-flux profiles (see Figs. 4 and 5) correspond to those of a largely "undisturbed" turbulent boundary layer. While it appears that the numerical solution predicts a thinner boundary layer than measured experimentally, the agreement is very good in the outer region. The calculations also suggest a high degree of flow symmetry in the outer flow at the upstream measurement locations, while the measured asymmetry was within the experimental uncertainty. At these upstream locations, the numerical results indicate that the flow in the boundary layer is moving slightly away from the centerline (Figs. 4d and 5d). The flow very near the body is being swept away from the centerline at a very high angle, indicating that the fin influences this part of the boundary layer.

Schlieren and shadowgraph photography[5,7] have indicated that this single WAF configuration produces a somewhat unsteady λ shock similar to that observed in front of blunt fins and cylinders in supersonic flow. Configurations possessing blunt leading edges have a stagnation point on the leading edge that corresponds to the end of a parting line in the flow, indicating the farthest location from the body at which particles become entrained into the vortical flow ahead of the leading

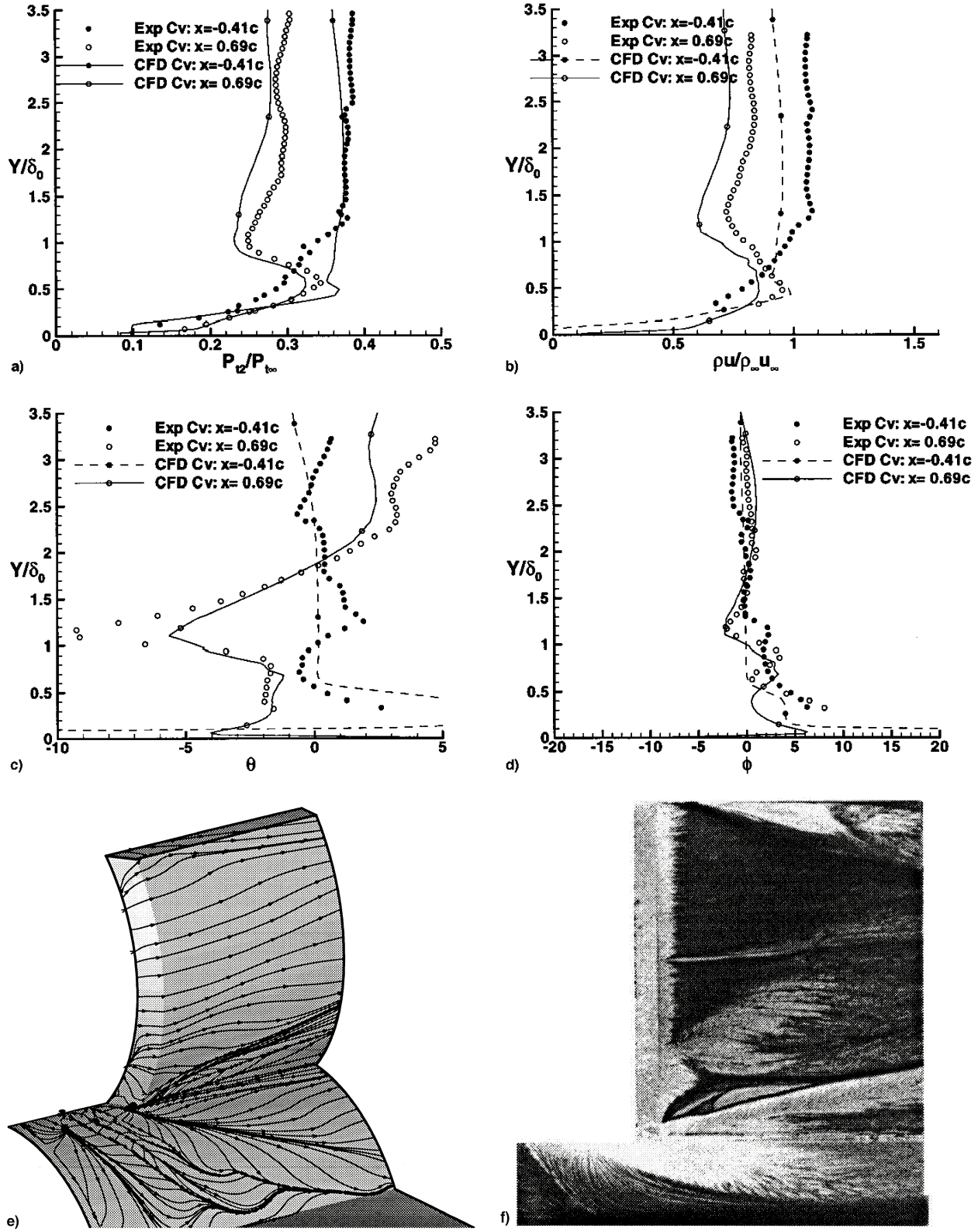

Fig. 4 Numerical and experimental flow variables; convex side of fin: a) $P_{t2}/P_{t\infty}$ (exp. ±1.2%), b) $\rho u/\rho_\infty/u_\infty$ (exp. ±11%), c) θ (deg, experimental uncertainty +15%), d) ϕ (deg, experimental uncertainty +15%), e) calculated limiting surface streamlines, and f) oil flow at Mach = 2.06.[14]

edge. The present test article has a sharp leading edge, making it difficult to identify any stagnation point in the CFD solutions. However, particle traces of the viscous CFD solution (Fig. 2) indicate that the distance from the body at which streamlines diverge as they encounter the fin leading edge is at $y \approx 0.19c$. This agrees quite well with the λ-shock height indicated by photography of $y \approx 0.20c$.[5,7,8]

Flow on the Convex Side of the Fin

As the flow nears the fin on the convex side, the outer flow ($Y/\delta_0 > 1.5$) passes through a strong shock (Fig. 6). This shock induces a strong compression and deceleration. As the fluid moves past the fin, it passes through a large region of favorable pressure gradient between the shock and the downstream measurement location (Fig. 6) primarily as a result of the convex

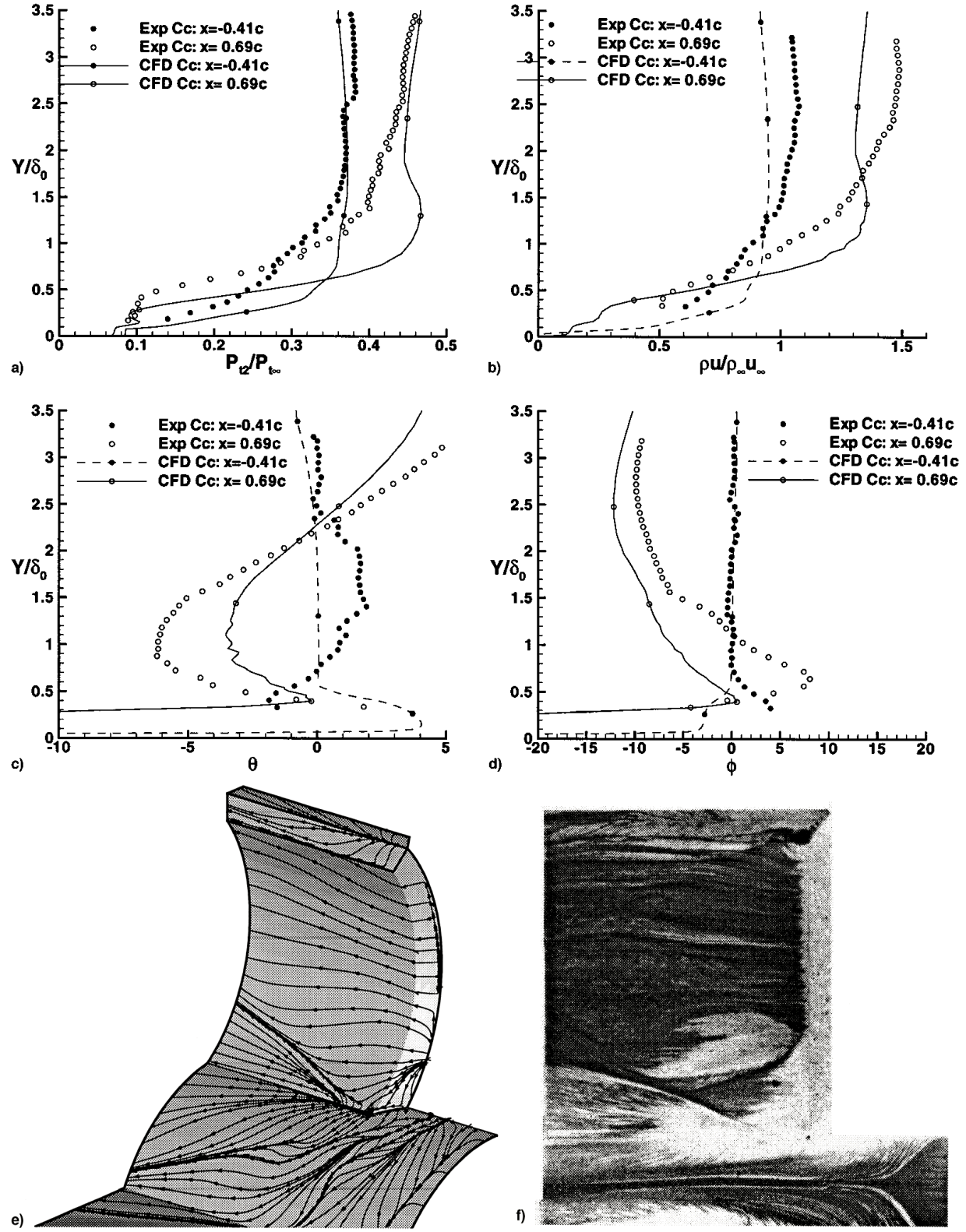

Fig. 5 Numerical and experimental flow variables; concave side of fin: a) $P_{t2}/P_{t\infty}$ (exp. ±1.2%), b) $\rho u/\rho_\infty/u_\infty$ (exp. ±11%), c) θ (deg, experimental uncertainty +15%), d) ϕ (deg, experimental uncertainty +15%), e) calculated limiting surface streamlines, and f) oil flow at Mach = 2.06.[14]

fin curvature. At the downstream survey location, the pitot pressure and mass-flux in the outer flow have been decreased on the convex side relative to the upstream reference plane (Figs. 4a and 4b). Profiles of pressure and momentum in the boundary layer at this location are characterized by large inflections (Figs. 4a and 4b). The flow near $Y/\delta_0 \approx 1.1$ has passed over the horseshoe vortex system produced by the shock/boundary-layer interaction ahead of the fin (Fig. 6). In this process, the flow greatly expands while only slightly accelerating; the net result is a decrease in the mass-flux. Flow in this region is directed strongly toward the body as indicated by the inflection in the horizontal flow angularity (Fig. 4c). Agreement with experimental data is considered excellent, although the flow turning angle is slightly underpredicted. Ex-

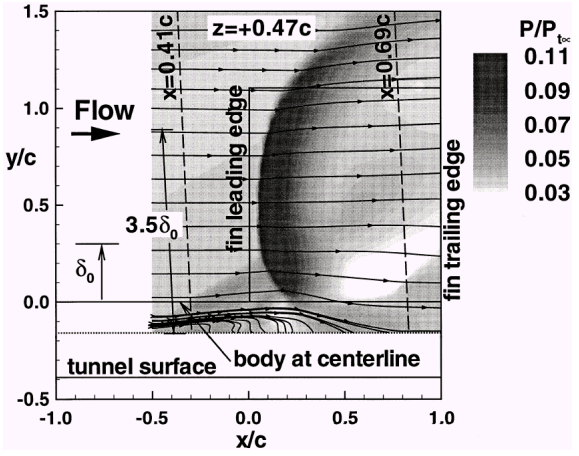

Fig. 6 Convex measurement plane ($z = +0.47c$) computed pressure levels and mass-flux streamlines (ρu, ρv). Outline of fin is overlaid. Dashed lines represent survey locations.

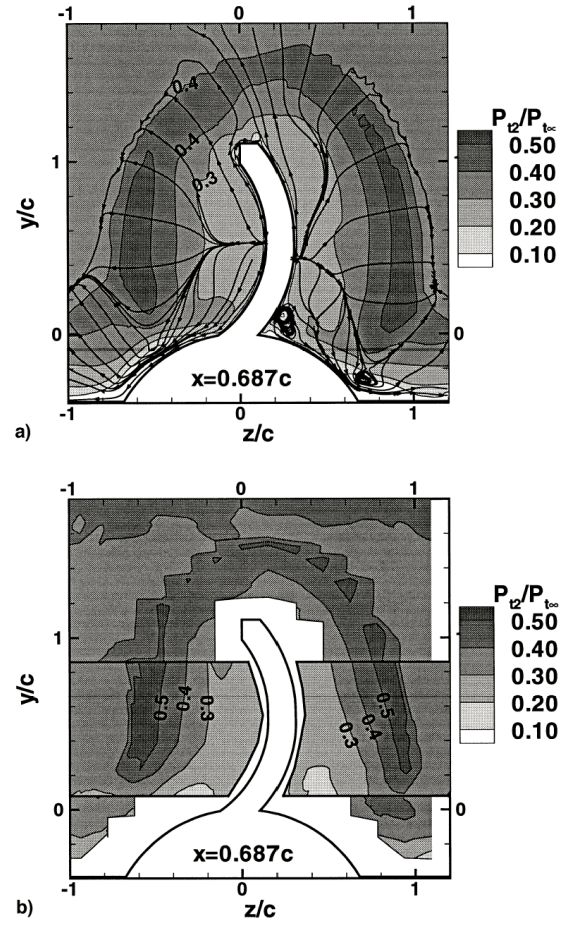

Fig. 7 Flow at $x = 0.69c$ measurement plane given by a) numerical pitot pressure and streamlines and b) experimental pitot pressure (±1.2%).

amination of the numerical results has revealed that this turning effect is caused by a vortex embedded in the fin/fuselage juncture that entrains fluid, pulling it toward the body (seen in Fig. 7a). This vortex also contributes to the pitot pressure inflections seen both numerically and experimentally in Fig. 4a. At roughly the same location, an inflection in the azimuthal flow angularity (ϕ) is observed (Fig. 4d). While the agreement between the numerical and experimental ϕ profiles is well within the uncertainty of the measurements, the predicted profiles for ϕ in this region were found to be influenced significantly by small errors in the survey location in the z direction.[7,8]

Slightly closer to the body ($0.3 < Y/\delta_0 < 1.0$), the flow experiences a compression from above while at the same time it is aligned with the x axis very near the body. The net effect is a sharp increase in mass-flux. The flattening of the θ profile in the experimental data over the range $0.3 < Y/\delta_0 < 0.8$ is closely duplicated numerically. Below $Y/\delta_0 \approx 0.3$, viscous effects force a decrease in mass-flux and pitot pressure. The flow is directed away from the fin over a very small region ($Y/\delta_0 < 0.2$), following the contour of the body. The numerical results and oil flow patterns at Mach 2.06[14] (discussed later) suggest that the azimuthal flow angularity, ϕ, at this location tends toward zero at the wall.

Given its proximity to the fin and, hence, its effects on the aerodynamic loading, more discussion on the juncture vortex is warranted. This vortex originates near the leading edge of the fin/root and remains tucked into the fin/body junction. The size and orientation of this vortex is clearly evident in limiting surface streamlines calculated from the numerical solution (Fig. 4e) and in the surface oil-flow patterns obtained by Abate and Berner[14] at Mach 2.06 (Fig. 4f). Surface streamlines starting at the leading edge travel downward along the beveled edge and join with streamlines flowing up from the root to form an accumulation of oil film (or convergence of streamlines) on the fin surface. This convergence marks the separation line formed by the juncture vortex, and moves away from the juncture as it travels toward the trailing edge. The complicated flow structure observed in the oil-flow patterns closely resembles that predicted by the numerical solution, suggesting that the flow structure near the juncture changes little within this Mach number range. On the body, a weak attachment line (surface streamline divergence) moving outward from the leading edge is clearly evident in both the numerical solution and the oil flow (cf. Figs. 4e and 4f).

Similar vortices have also been inferred from oil-flow patterns on straight blunt fins mounted on flat plates,[15,16] where modest changes in fin incidence have been observed to actually change rotational direction of the vortex. Thus, with respect to the juncture vortex, fin curvature and attachment angle can induce similar effects to those produced by crossflow.

Flow on the Concave Side of the Fin

In contrast to the flow on the convex side of the fin, the flow on the concave side passes through a somewhat weaker shock (Fig. 8). Thus, the flow undergoes a much more modest deceleration. Also, the postshock expansion is partially offset by the compressive effects of fin curvature. The net effect is a dramatic increase in the mass-flux (up to 30%) at the downstream measurement location as compared with the upstream

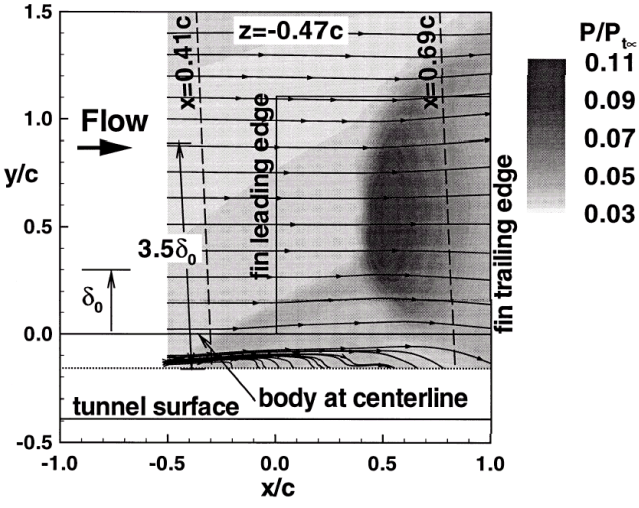

Fig. 8 Concave measurement plane ($z = -0.47c$) computed pressure contours and mass-flux streamlines (ρu, ρv). Outline of fin is overlaid. Dashed lines represent survey locations.

location. This increase is observed in numerical and experimental data. On this side of the fin, the outer flow is strongly directed away from the fin (Fig. 5d) at flow angles, ϕ, up to 10 deg at the midspan ($Y/\delta_o \approx 2.5$). Here, numerical and experimental results indicate that $\theta \approx 0$ deg, meaning that the flow is directed toward the center of fin curvature (Figs. 5c and 7a).

Approaching the body, the fluid momentum decreases (Figs. 5a and 5b). The overprediction of the pitot pressure and momentum in the outer boundary layer on this side of the fin is probably the result of the lack of pressure gradient effects in the algebraic turbulence model. As we have reported previously,[8] the turbulence levels on this side of the fin are highly attenuated, leading to significant turbulent shear stresses. Over a small region inside the boundary layer ($0.5 < Y/\delta_o < 1.0$), the numerical solution suggests that there is a large inflection in the azimuthal angularity (Fig. 5d), where the flow is almost aligned with the vertical plane ($\phi \approx 0$ deg). This inflection is even more pronounced in the experimental data, and is probably produced by a combination of the flow wrapping around the fin and an expansion that reflects off of the bow shock as a compression. Inviscid numerical results also hinted (faintly) at this trend.[5,6,8] Over this same range, the experimental and numerical data (Fig. 5c) suggest that the magnitude of the horizontal flow angularity is greatly reduced.

Closer to the body ($Y/\delta_o < 0.5$) there is a small region in which measured and computed pitot pressures do not change. The downstream measurement station on this side of the fin is located just behind a separation on the body, which is seen in the computational results and oil-flow pattern. The numerical results suggest that the flow is moving downward and away from the fin ($\theta \approx -30$ deg, $\phi \approx -39$ deg), though cross-wire volume effects precluded detailed experimental examination of this region.[6,8] On this side of the fin, surface streamlines starting at the leading edge also travel downward along the beveled edge and join with streamlines flowing up from the root. However, the streamline convergence is incomplete from below, and no juncture vortex is indicated on this side of the fin, in either the numerical or experimental studies, nor is one indicated by the oil-flow visualizations[14] at Mach 2.06 (Figs. 5e and 5f). Presumably, this is largely attributable to the oblique attachment angle ($\approx$135 deg). As on the convex side, the similarities between the predicted surface streamlines and the observed oil-flow patterns of Abate and Berner[14] at Mach 2.06 suggest that the flow structure near the juncture on this side of the fin changes little within this Mach number range.

Aerodynamic Loading on the Fin

The diverse flow topologies on either side of the WAF produce dramatically different load distributions on the opposing fin surfaces. While previous inviscid calculations[3,5] have captured many of the essential flow features, the flow near the fin/body juncture is dominated by viscous effects and can produce significant changes in aerodynamic load.

On the concave side of the fin, the fin curvature creates a large region of relatively high surface pressures (Fig. 9), near the half-span that contributes to the negative rolling moment typically experienced in supersonic flight. Previous inviscid calculations also predicted a region of high pressure near the fin root on the convex side,[5] where pressure levels were near the magnitudes predicted on the concave side. This compression was initially attributed to the fin attachment angle ($\approx$45 deg). However, the present viscous numerical results show that this high-pressure region is displaced away from the body, and significantly weakened by viscous phenomena (Fig. 9a). The root region is characterized instead by low pressures induced by the juncture vortex.

It has been previously shown using Euler methods[3] that the rolling moment is a function of both the fin curvature and fin attachment angle. However, it is now clear that the effects of such fin asymmetries cannot be fully captured by an inviscid

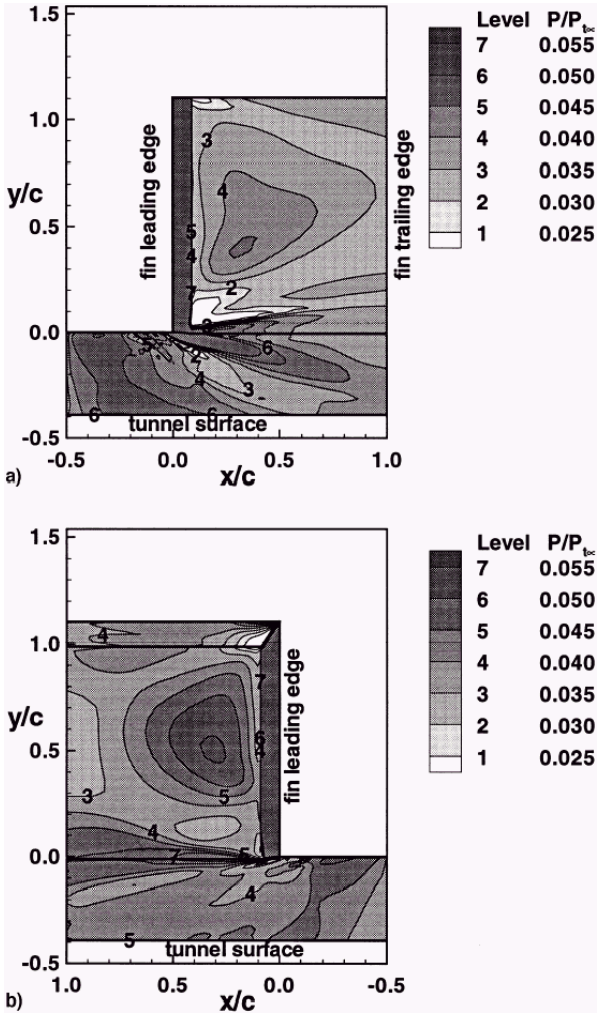

Fig. 9 Computed fin surface pressures: a) convex and b) concave sides.

analysis. In the present case, this can be illustrated by examining the predicted rolling moment. The present viscous CFD predicts a 10% greater rolling moment (-0.0112) than an inviscid analysis[5] (-0.0102) conducted on the same single-WAF geometry. This variation is entirely a result of the considerable differences in the fin pressure distributions predicted by the two methods, most notably those induced by the juncture vortex.

Conclusions

The Reynolds-averaged Navier–Stokes equations have been solved with the Baldwin–Lomax algebraic turbulence model in the vicinity of a single WAF mounted on a semicylindrical body. The excellent agreement with experimental data suggests that the calculations have captured the salient features of this complicated flowfield. It is notable that the oil-flow pattern to which these results compared so favorably was obtained on a four-finned missile. Thus, the resemblance of computed and observed surface streamline patterns on the fin suggests that the simplified single-fin model produces the relevant flow features in the fin region for a nonspinning missile with multiple WAFs.

One of the more significant findings of the present study is that both inviscid and viscous properties play significant roles in determining the structure of the flowfield near WAFs. The outer flowfield exhibits asymmetries brought about by the effects of pressure gradient, streamline curvature, and differing shock/expansion structures, whereas viscous phenomena induce asymmetries closer to the body. Regarding the latter, the

present Navier–Stokes simulations predicted a vortex in the fin/body juncture on the convex side of the fin. The existence of this viscous-induced vortical structure was corroborated by both hot-film anemometry and surface flow visualizations. This vortex, not present on the concave side, presumably due to the oblique fin attachment angle, influences the pressure loading near the fin root. The net result is a pressure differential across the fin that alters the rolling moment. It is known that the structure and strength of such juncture vortices can be changed by any of several factors, including the incidence angle of the fin. Such a change could greatly influence the rolling moment, possibly to the point of a reversal. Inviscid numerical simulations cannot produce this vortex and, thus, may not be expected to reasonably predict the stability behavior of missiles having WAFs.

Acknowledgment

The authors would like to thank Gregg Abate of the U.S. Air Force Research Laboratory's Munitions Directorate for sponsoring this work.

References

[1]Abate, G. L., "Aerodynamic Research of Wrap Around Fin Missile Configurations and Alternative Wrap Around Fin Designs," Wright Laboratory, WL-TR-94-7015, Feb. 1994.

[2]Vitale, R. E., Abate, G. L., Winchenbach, G. L., and Riner, W., "Aerodynamic Test and Analysis of a Missile Configuration with Curved Fins," AIAA Paper 92-4495, Aug. 1992.

[3]Abate, G. L., and Cook, T., "Analysis of Missile Configurations with Wrap-Around Fins Using Computational Fluid Dynamics," AIAA Paper 93-3631, Aug. 1993.

[4]Edge, H. L., "Computation of the Roll Moment for a Projectile with Wrap-Around Fins," *Journal of Spacecraft and Rockets*, Vol. 31, No. 4, 1994, pp. 615–620.

[5]Tilmann, C. P., Huffman, R. E., Jr., Buter, T. A., and Bowersox, R. D. W., "Characterization of the Flow Structure in the Vicinity of a Wrap-Around Fin at Supersonic Speeds," AIAA Paper 96-0190, Jan. 1996.

[6]Huffman, R. E., Jr., Tilmann, C. P., Buter, T. A., and Bowersox, R. D. W., "Experimental Flow Structure Investigation of a Wrap-Around Fin at Mach 2.9," AIAA Paper 96-2450, June 1996.

[7]Tilmann, C. P., "Numerical and Experimental Investigation of the Flowfield near a Wrap-Around Fin," Ph.D. Dissertation, Air Force Institute of Technology (AU), AFIT/DS/ENY/97-1, Wright–Patterson AFB, OH, March 1997.

[8]Tilmann, C. P., Huffman, R. E., Jr., Buter, T. A., and Bowersox, R. D. W., "Experimental Investigation of the Flow Structure near a Single Wrap-Around Fin," *Journal of Spacecraft and Rockets*, Vol. 34, No. 6, 1997, pp. 729–736.

[9]Tilmann, C. P., Buter, T. A., and Bowersox, R. D. W., "Characterization of the Flowfield near a Wrap-Around Fin at Mach 2.8," AIAA Paper 97-0522, Jan. 1997.

[10]*GASP Version 3—The General Aerodynamic Simulation Program—User's Manual*, Aerosoft, Inc., Blacksburg, VA, May 1996.

[11]Baldwin, B. S., and Lomax, H., "Thin Layer Approximation and Algebraic Model for Separated Turbulent Flow," AIAA Paper 78-0257, Jan. 1978.

[12]Miller, R., Dotter, J., Bowersox, R. D. W., and Buter, T. A., "Compressible Turbulence Measurements in Supersonic Boundary Layers with Favorable and Adverse Pressure Gradients," *ASME Transitional and Turbulent Flows*, FED-Vol. 224, 1995, pp. 193–200.

[13]Van Leer, B., "Flux-Vector Splitting for the Euler Equations," *Lecture Notes in Physics*, Vol. 170, 1982, pp. 507–512.

[14]Abate, G. L., and Berner, C., "Wind Tunnel Measurements Wrap-Around Fins at Mach 2.06," AIAA Paper 94-3499, Aug. 1994.

[15]Dolling, D. S., and Bogdonoff, S. M., "Blunt Fin-Induced Shock Wave Turbulent Boundary Layer Interaction," *AIAA Journal*, Vol. 20, No. 12, 1982, pp. 1674–1680.

[16]Fomison, N. R., and Stollery, J. L., "The Effects of Sweep and Bluntness on a Glancing Shock Wave Turbulent Boundary Layer Interaction," AGARD-CP-428, NATO, Nov. 1987, pp. 1–18.